Complex non-linear phenomena and stability analysis of interconnected power converters used in distributed power systems

Abdelali El Aroudi[1], Damian Giaouris[2] ✉, Kuntal Mandal[3], Soumitro Banerjee[3],
Mohammed Al-Hindawi[4], Abdullah Abusorrah[4], Yusuf Al-Turki[4]

[1]Department of Electronics, Electrical Engineering and Automatic Control, Rovira i Virgili University, Tarragona, Saint Barthélemy
[2]Laboratory of Process Systems Design and Implementation, Centre for Research and Technology Hellas, Thessaloniki, Greece
[3]Physical Science, IISER Kolkata, Kalyani, India
[4]Department of Electrical and Computer Engineering, King Abdulaziz University, Jeddah, Saudi Arabia
✉ E-mail: Damian.Giaouris@ncl.ac.uk

Abstract: Distributed power systems are considered to be a key element of future power grids. Their main characteristic is the local production and consumption of energy that is accomplished using a number of power converters that interconnect local sources and loads. In this paper, a current mode controlled dc–dc converter which feeds another current mode controlled dc–dc converter is considered to meet the demands of the load. It shows that the existence of the second converter at the output has destabilising effect on the overall system. Such a system may also exhibit interactions of various types of instability that conventional modeling methods cannot predict. Slow-timescale oscillation in standalone switching converters is usually attributed to the occurrence of a Neimark–Sacker bifurcation of the fundamental periodic orbit of the discrete-time model of the system. But in the studied cascaded system, the underlying mechanism is quite different. This paper fully explains the mechanisms as well as the conditions of the occurrence of such instabilities by employing the analytical and numerical tools of the exact switched model of the system. These results can be useful for developing design guidelines to avoid such problems. Finally, the results have been validated experimentally.

1 Introduction

While existing electrical grids are designed for centralised power generation, distributed power systems (DPSs), with renewable energy sources, are changing this paradigm. In DPS, photovoltaic arrays, wind turbines and batteries are used to feed a main (dc or ac) bus connected to its loads, as well as the utility grid, forming the so-called nanogrid or microgrid [1].

Owing to their modular approach, DPS have many advantages compared with a conventional centralised power system such as higher efficiency, better reliability, higher power density, faster response and better standardisation. In these applications, instead of using a single bulky power supply to provide the final voltages/ currents required by the load, the power processing tasks are distributed among many power processing modules, i.e. several power converters are connected together either in series, cascade or in parallel. One of the major requirements in such power networks is that the overall system is stable and operates with high efficiency.

The stability analysis of cascaded switching converters can be dated back to the input filter designs of switching regulators in 1970s when it was observed that an input filter added to a buck converter leads to a change of the original control loop gain and finally to performance degradation [2, 3] which can be predicted by using the minor loop gain (MLG), i.e. the ratio of the output impedance of the source converter to the input impedance of the load downstream converter. However, obtaining the total loop gains in addition to the MLG is a tedious task because both the output impedance for the upstream first stage and the input impedance for the downstream second stage are needed in addition to the two separate total loop gains of the two cascaded converters [3]. Furthermore, this type of linear analysis cannot predict many of the non-linear phenomena that the system can exhibit. Non-linear average modelling and analysis have been used in [4] to study the dynamical behaviour of cascade-interconnected

converters. A bifurcation approach has been used in [5] where Hopf bifurcation has been accurately predicted for two cascaded buck converters under voltage mode control (VMC). Similar behaviour has been reported in [4, 6] for a cascaded system in which the second stage under a VMC was approximated by constant power load and an averaged modelling approach was used to predict the dynamical behaviour of the complete system. Since averaged models were used in the earlier works, only slow-scale instability phenomena have been analysed.

On the other hand, during the past couple of decades, much effort has been devoted to the study of both fast-scale and slow-scale non-linear behaviours in single dc–dc switching converters [5, 7– 13]. A large variety of different complex non-linear instability phenomena such as period doubling (PD) leading to subharmonic oscillations and chaotic behaviour characterised by an undesirable large current ripple [7, 8], Hopf (or Neimark–Sacker) bifurcations leading to extra low-frequency high amplitude oscillation [10] and saddle-node (SN) bifurcation [11] due to coexistence of different steady-state solutions have been reported in switched-mode dc–dc converters. These studies, which are mostly based on accurate approaches such as discrete-time mappings [7, 8] or the Floquet theory together with *Filippov's method* [13], allow a deep understanding of the fundamental properties describing the non-linear dynamic behaviour of these systems.

Part of previous studies has focused on the mechanisms by which bifurcations can lead to the appearance of quasi-periodic or mode-locked periodic dynamics as a pair of complex conjugate Floquet multipliers (eigenvalues for the discrete-time mapping) of a stable periodic orbit crosses the unit circle in the complex plane. Such a process represents a Neimark–Sacker bifurcation of the discrete-time model of the switching converter. This is the case, for instance, of the cascaded buck converter considered in [5], the current mode controlled cascaded boost converter in [14], the cage induction motor drive system [15], the multilevel buck converter [10] and the dc power networks for transportation systems [16].

Interaction of the torus with PD instability has also been reported recently in [17–20] where different interaction mechanisms have been identified.

On the one hand, there have been many research efforts devoted to stand-alone and paralleled dc–dc converters [21] using non-linear techniques. Many researchers have investigated cascaded converters using conventional linear techniques [22–25]. The objective of the present paper is to apply the recently developed non-linear analysis techniques to cascaded converters.

Some initial study by the authors was presented in [26]. In the present paper, we thoroughly study and expand the previous analysis and fully explain the originally reported phenomena which are different from that of a stand-alone buck converter loaded by a constant resistance. First, it will be shown that the system may present some complex phenomena due to the interaction of the two stages. In particular, it will be shown that when a buck converter under a peak current mode control (PCMC) is loaded by a boost converter under a type-II average current mode control (ACMC), the well-known subharmonic oscillation that occurs in stand-alone converters, does not occur. Instead, a coexistence of fast-scale and slow-scale instabilities takes place. Such interactions between bifurcations have also been reported in other publications (see [17, 18]). We show that in this system the mechanism of the interaction between fast- and slow-scale dynamics is completely different.

The rest of this paper is organised as follows: Section 2 deals with the description of the system under study. The bifurcation phenomena exhibited by the system are shown in Section 3 and then explained in Section 4 in terms of Floquet multipliers, corresponding to different kinds of T-periodic and $2T$-periodic orbits. Design-oriented stability boundaries are plotted in the same section. The bifurcation scenario responsible for the interaction is also explained. In Section 5, we use a laboratory prototype of cascaded buck–boost converter to experimentally show the occurrence of interaction of different types of instabilities. Finally, some concluding remarks are presented in the last section.

2 Current mode controlled interconnected buck and boost converters

2.1 System description

In this paper, a two-stage dc–dc power converter is considered (Fig. 1) which consists of a cascade connection of a buck converter acting as a line conditioner and a boost converter acting as a point of load converter under an ACMC for supplying a load requiring a regulated current instead of a regulated voltage. In modelling the system, the switches and diodes are considered ideal and the equivalent series resistances (ESRs) of inductors and capacitors are included. By applying Kirchoff's current and voltage laws to the circuit depicted in Fig. 1, the system can be described by the following set of equations

$$\frac{dv_{C1}}{dt} = \frac{i_{L1} - i_{L2}}{C_1} \tag{1a}$$

$$\frac{di_{L1}}{dt} = \frac{v_g}{L_1}u_1 - \frac{v_{C1}}{L_1} - \frac{r_{L1}i_{L1}}{L_1} - \frac{r_{C1}(i_{L1} - i_{L2})}{L_1} \tag{1b}$$

$$\frac{dv_{C2}}{dt} = \frac{\kappa_2 i_{L2}}{C_2}(1 - u_2) - \frac{v_{C2}}{C_2(R + r_{C2})} \tag{1c}$$

$$\frac{di_{L2}}{dt} = \frac{v_{C1}}{L_2} + \frac{r_{C1}(i_{L1} - i_{L2})}{L_2} - (1 - u_2)\kappa_2\left(\frac{v_{C2}}{L_2} + \frac{r_{C2}i_{L2}}{L_2}\right)$$
$$- \frac{r_{L2}i_{L2}}{L_2} \tag{1d}$$

where v_{C1}, i_{L1}, v_{C2} and i_{L2} are the state variables of the power stage that stand for the capacitor voltages and the inductor currents in the first and the second stages, respectively. The variables u_1 and u_2 are the binary command signals used to drive the switches S_1 and S_2, respectively, R is the load resistance of the second stage and v_g is the input voltage of the first stage. L_1, L_2, C_1 and C_2 are the inductances and the capacitances of the first and the second stages, r_{L1}, r_{L2}, r_{C1} and r_{C2} being their ESRs and $\kappa_2 = R/(R + r_{C2})$.

The inductor current in the first stage is being controlled by a typical peak current mode controller (PCMC) with an artificial T-periodic ramp compensator $i_{a1}(t)$ with slope m_{a1}. Since boost converters are non-minimum phase systems when output variables are fed back, direct output control is problematic, and therefore in this paper we control the inductor current using a tight ACMC in order to compensate for any load or input changes. In this case, the inductor current i_{L2} is sensed and the error $i_{ref2} - i_{L2}$ is processed by a current compensator whose transfer function $G_c(s)$ contains a pole at the origin to remove the steady-state error, a real pole $-\omega_p$ at one half switching frequency to remove switching noise and a real zero $-\omega_z$ ($\omega_z \ll \omega_p$) to increase the phase margin at the cross-over frequency. The control signal v_{con2} is generated at the output of this compensator and then is compared with an external T-periodic sawtooth ramp modulator $v_{r2} = m_{a2}(t \bmod T)$ with a slope m_{a2}. The compensator can be described in the Laplace s-domain by

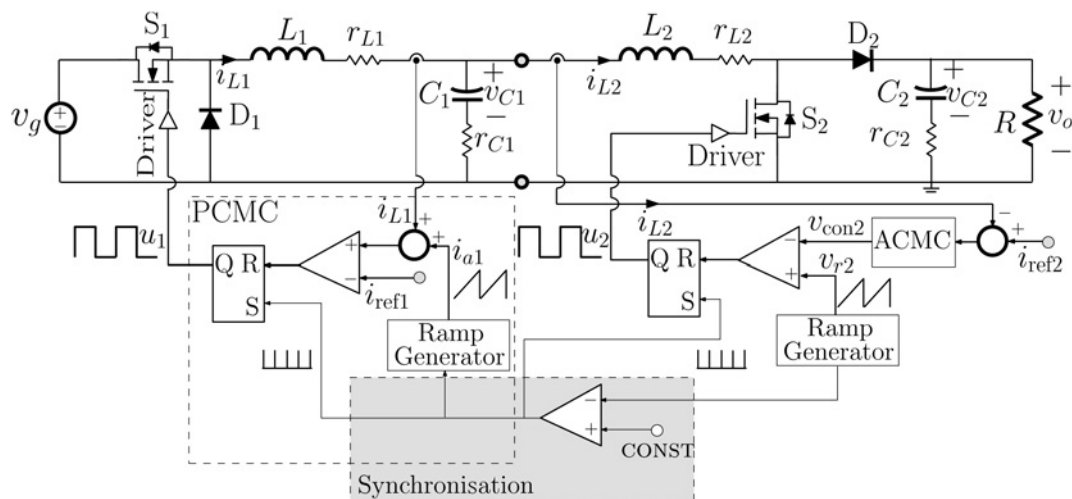$$G_c(s) = \frac{W(s + \omega_z)}{s(s + \omega_p)} \tag{2}$$

Fig. 1 *Buck converter loaded by boost converter both under CMC*

where W is a suitable constant gain. Transforming this s-domain model to the state-space time-domain, the current controller can be described by the following set of differential equations

$$\frac{dv_p}{dt} = v_z, \qquad \frac{dv_z}{dt} = i_{ref2} - i_{L2} - \omega_p v_z \qquad (3)$$

where v_p and v_z are the state variables of the compensator. The control signal v_{con2} for the second stage can be expressed in terms of these two additional variables as

$$v_{con2} = W(\omega_z v_p + v_z) \qquad (4)$$

In continuous conduction mode (CCM), four different configurations C_1, C_2, C_3 and C_4 are possible, corresponding, respectively, to the pair states (ON, ON), (OFF, ON), (ON, OFF) or (OFF, OFF) of the switches S_1 and S_2. However, during a switching period, the system can switch among only three of them as the configuration $C_2 := $ (OFF, ON) or $C_3 := $ (ON, OFF) is skipped depending on whether $D_1 < D_2$ or $D_2 < D_1$, where D_1 and D_2 are the duty cycles of the first stage and the second stage, respectively. In the first stage, the switching instances are decided by comparing the inductor current i_{L1} to the signal $i_{ref1} - m_{a1}(t \bmod T)$ and in the second stage by comparing the control voltage v_{con2} with the T-periodic ramp modulator $v_{r2} = m_{a2}(t \bmod T)$. Therefore, the switch S_1 in the first stage is closed at the beginning of each clock period and is turned OFF whenever the switching function

$$\sigma_1(\boldsymbol{x}, t) := i_{ref1} - m_{a1}(t \bmod T) - i_{L1} \qquad (5)$$

is equal to zero. In the second stage the switching condition is given by

$$\sigma_2(\boldsymbol{x}, t) := W\omega_z v_p + Wv_z - m_{a2}(t \bmod T) = 0 \qquad (6)$$

The controllers in both stages are synchronised by sharing the same clock signal between their respective modulators. This signal is generated from a comparator whose inputs are the ramp modulator in the second stage and a small constant voltage marked as CONST in Fig. 1.

For each state of the switch pair (S_1, S_2), the system can be described by a set of linear differential equations that can be written as $\dot{\boldsymbol{x}} = \boldsymbol{A}_{ij}\boldsymbol{x} + \boldsymbol{B}_{ij}, (i, j) \in \{0, 1\}^2$. Obtaining $\boldsymbol{A}_{ij}$ and $\boldsymbol{B}_{ij}$ from (1a)–(1d) and (3) is straightforward.

Different types of T-periodic cycles are possible for the system depending on the parameters of the first and the second stages. These different T-periodic orbits define different operating modes for the system depending on the relationship between the duty cycles of the driving signals, the switching frequency, values of the inductors and the load resistance. However, if both the stages operate in CCM, it can be shown that there are basically two operating modes that can be summarised as follows:

- *Mode 1*: if $D_1 < D_2$, the switching sequence during one complete switching period is

$$C_1 \rightarrow C_2 \rightarrow C_3 \rightarrow C_1 \rightarrow C_2 \rightarrow C_3 \rightarrow \cdots \qquad (7)$$

For this mode, configuration C_4 is skipped.

- *Mode 2*: if $D_1 > D_2$, the switching sequence becomes

$$C_1 \rightarrow C_4 \rightarrow C_3 \rightarrow C_1 \rightarrow C_4 \rightarrow C_3 \rightarrow \cdots \qquad (8)$$

For this mode, configuration C_2 is skipped.

3 Possible instabilities in the system

In this section, we investigate the possible mechanisms of instability and the resulting dynamical behaviours.

The circuit parameter values used in this section are shown in Table 1 and they are representative of practical DPS operating in CCM. The input voltage considered is in the range between 50

Table 1 Parameter values used in the first and second stages

L_1, r_{L1}	C_1, r_{C1}	m_{a1}		
37.5 μH, 10 mΩ	420 μF, $r_{C1} = 50$ mΩ	10 kA/s		
L_2, r_{L2}	C_2, r_{C2}	R	W, ω_z, ω_p	m_{a2}
200 μH, 10 mΩ	200 μF, 20 mΩ	10 Ω	78.5, 10, 157 krad/s	2500 kV/s

and 120 V with an average input current between 40 and 56 A which means that the power is in the range between 2 and 6.7 kW. The allowed ripple in the inductor current in nominal stable operation is about 20% while in the intermediate and the output capacitor voltages is <1%. The switching frequency is $f_s = 50$ kHz. This parameter is selected equal for both converters to avoid added complexities due to possible switching frequency interaction.

In such systems, it is of practical interest to examine the dynamical behaviour of the system when the current references i_{ref1}, i_{ref2} and the input voltage v_g vary. Fig. 2 shows the steady-state response of the system for $i_{ref2} = 38$ A, $v_g = 120$ V and different values of i_{ref1}, obtained using PSIM circuit simulator. For $i_{ref1} = 45$ A, the system exhibits a stable T-periodic behaviour in Mode 1. If $i_{ref1} = 48$ A, the T-periodic orbit loses its stability and we see a combination of slow-scale and fast-scale oscillations. Note the dramatic increase of the current ripple of i_{L1} that can have catastrophic consequences in the overall system's performance and efficiency. Similar 'coexistence' of slow-scale and fast-scale oscillations has been reported earlier [17], but we shall show in the following sections that in this case the pathway to such behaviour is completely different.

To understand the mechanisms of the creation of this behaviour, a bifurcation diagram for the system is plotted by considering the demanded current i_{ref1} (a similar pattern is obtained using i_{ref2} or v_g), Fig. 3a. To better understand Fig. 3a and to illustrate how the trajectory of the system is evolving, the samples $i_{L1}(2nT)$ at even multiples of the switching period are plotted in dark colour while those at odd multiples of the switching period $i_{L1}((2n+1)T)$ are plotted in light colour.

The corresponding discrete-time state-space trajectory for $i_{ref1} = 46.1$ A is shown in Fig. 3b. From the bifurcation diagram in Fig. 3a, it can be observed that for $i_{ref1} < 46.1$ A approximately, the system exhibits a stable periodic behaviour. At $i_{ref1} \simeq 46.1$ A, the system periodic regime loses its stability and the attractor of the system evolves on a *two-loop* attractor (Fig. 3b) manifesting itself as a single band in the bifurcation diagram. As the bifurcation parameter is increased, the two loops of the torus get smaller and smaller and are disconnected at a critical value of $i_{ref1} \simeq 47$ A. As i_{ref1} is increased, the loops shrink to two points at $i_{ref1} \simeq 54$ A, and subsequently a one-band chaotic attractor develops.

4 Stability analysis using Floquet theory and Filippov method

In the previous section, we saw that a stable T-periodic orbit loses stability at approximately $i_{ref1} = 46.1$ A and a torus whose Poincaré section is a two-loop curve is created. In this section using Filippov's method we further investigate the observed non-linear phenomena. To do that we obtain the location of the fixed points and the eigenvalues of the monodromy matrix [12, 13]. For $i_{ref1} < 46.1$ A we see that, apart from the previously observed T-periodic orbit, there exists one more unstable (saddle) periodic orbit. It is also found that initially the saddle is operating in Mode 2 and then changes to Mode 1. This event, however, has no notable effect on the operation of the system.

Table 2 shows the Floquet multipliers of two different fixed points corresponding to the T-periodic orbit in Mode 1 [see (7)] and Mode 2 [see (8)] as the bifurcation parameter i_{ref1} is varied in the vicinity of the critical value $i_{ref1} \simeq 46.1$ A. As i_{ref1} is increased, one eigenvalue of the saddle (which is >1) approaches 1 from above. At the same time, one eigenvalue of the node which was <1, approaches 1 from below. At approximately $i_{ref1} = 46.1$ A, these two fixed points
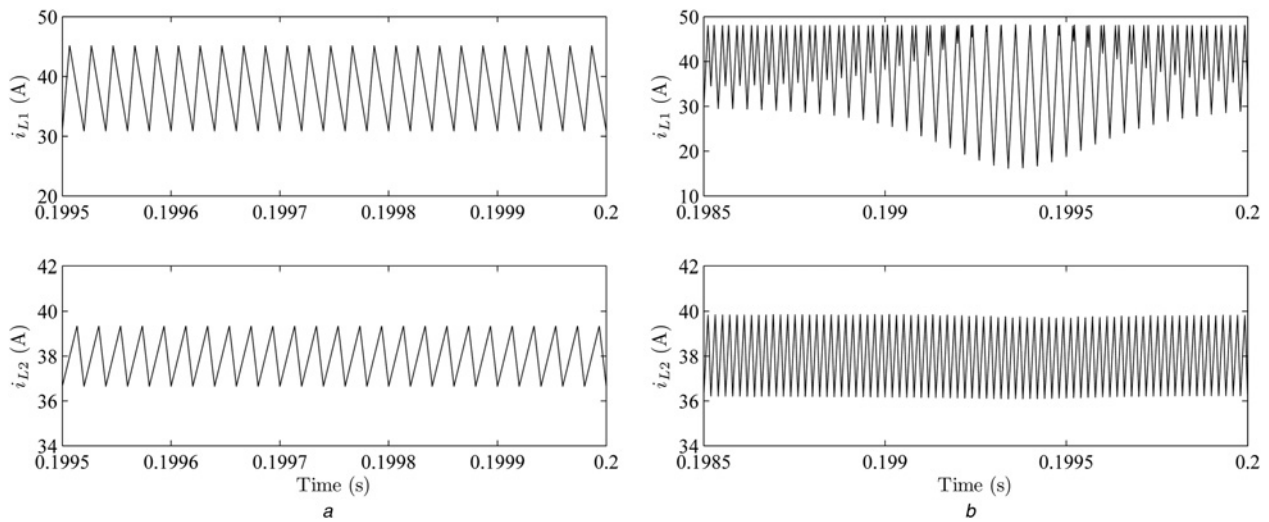
Fig. 2 *Waveforms of the inductor currents i_{L1} and i_{L2} before and after losing stability due to variation in the current reference i_{ref1}*

a i_{ref1} = 45 A: stable in Mode 1
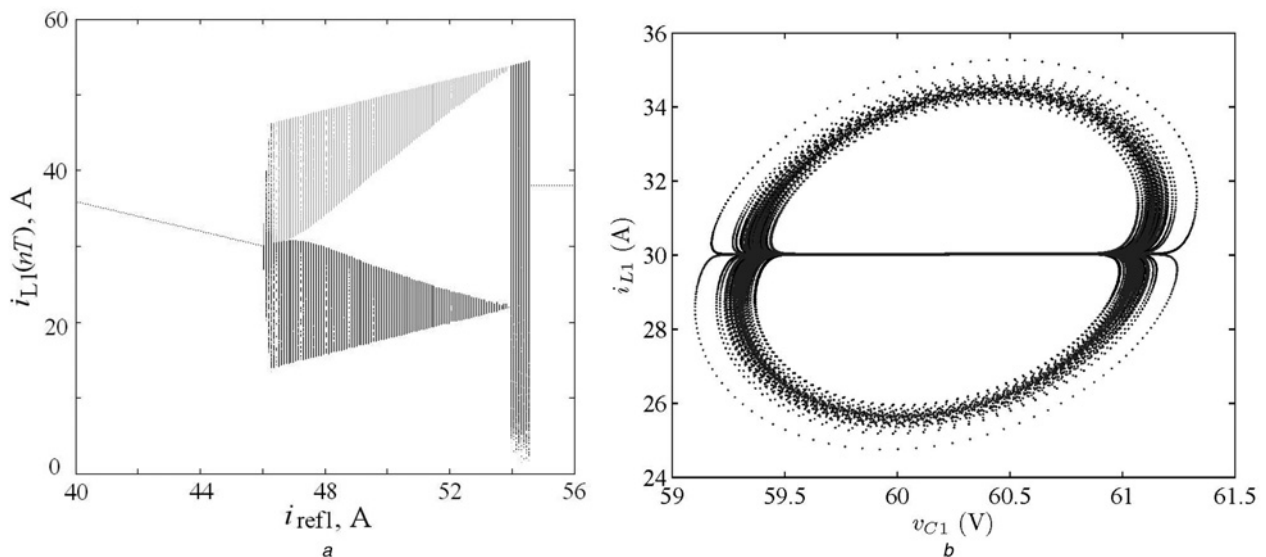*b* i_{ref1} = 48 A: interacting fast-scale and slow-scale instabilities

Fig. 3 *Response of the system under parameter change that highlight the observed instabilities*

a Bifurcation diagram obtained from sampling the state variables of the switched system. Dark colour represents the samples $i_{L1}[(2n + 1)T]$ at odd multiples of the switching period while light colour represents the samples $i_{L1}(2nT)$ at even multiples of the switching period
b Sampled state variables of the system in the plane (v_{C1}, i_{L1}) (stroboscopic Poincaré section) showing a two-loop trajectory resulting from the complex interaction of slow-scale and fast-scale instabilities

Table 2 Floquet multipliers of the *T*-periodic orbits in the vicinity of the SN bifurcation

i_{ref1}, A	Mode	Floquet multipliers	Stability
44.00	Mode 1	(−0.3175, 0.1563 ± 0.1795*j*, 0.7679, **0.9943**, 0.9809)	stable
	Mode 2	(−3.0294, − 0.0121 ± 0.2344*j*, 0.7885, *1.0058*, 0.9807)	saddle
45.00	Mode 1	(−0.4513, 0.1161 ± 0.2065*j*, 0.7748, **0.9958**, 0.9808)	stable
	Mode 2	(−2.1287, 0.0018 ± 0.2349*j*, 0.7874, *1.0042*, 0.9807)	saddle
45.50	Mode 1	(−0.5598, 0.0941 ± 0.2169*j*, 0.7779, **0.9969**, 0.9808)	stable
	Mode 2	(−1.7146, 0.0121 ± 0.2347*j*, 0.7866, *1.0031*, 0.9807)	saddle
45.90	Mode 1	(−0.7128, 0.0720 ± 0.2247*j*, 0.7806, **0.9982**, 0.9808)	stable
	Mode 2	(−1.3448, 0.0257 ± 0.2338*j*, 0.7854, *1.0018*, 0.9807)	saddle
46.00	Mode 1	(−0.7828, 0.0641 ± 0.2270*j* 0.7815, **0.9987**, 0.9807)	stable
	Mode 1	(−1.2243, 0.0315 ± 0.2332*j*, 0.7848, *1.0013*, 0.9807)	saddle
46.05	Mode 1	(−0.8358, 0.0588 ± 0.2283*j*, 0.7821, **0.9991**, 0.9807)	stable
	Mode 1	(−1.1468, 0.0358 ± 0.2326*j*, 0.7844, *1.0009*, 0.9807)	saddle
46.1	Mode 1	(−0.8027, 0.0621 ± 0.2275*j*, 0.7817, **0.9989**, 0.9807)	stable
	Mode 1	(−0.9937, 0.0457 ± 0.2310*j*, 0.7834, *1.0001*, 0.9807)	saddle
46.2	–	no existence of *T*-periodic solutions	–

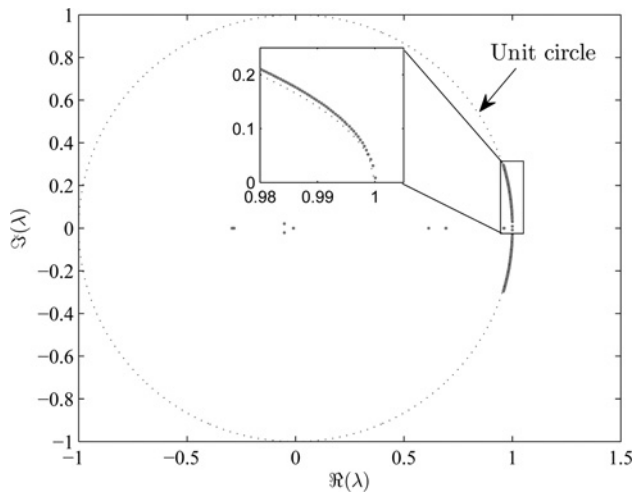Bold characters indicate the SN bifurcation, while the italics the PD.

Fig. 4 *Loci of the Floquet multipliers corresponding to the 2T-periodic orbit as the parameter i_{ref1} is varied in the range (46.1, 54) A*

collide and are destroyed in an SN bifurcation. Something interesting happens to the 'invisible' saddle orbit before it disappears in the SN bifurcation. At $i_{ref1} = 44$ A, the saddle has an eigenvalue at −3.0294, and as i_{ref1} increases this eigenvalue moves toward −1. It crosses −1 between 46.05 and 46.1 A, indicating that a PD bifurcation takes place, creating two new branches of a 2T-periodic orbit. This PD bifurcation is of a sub-critical nature, as the 2T-periodic orbit exists in the side where one of the eigenvalues of the T-periodic orbit goes inside the unit circle.

The unstable 2T-periodic orbit, that is born out of the unstable T-periodic orbit, plays an important role in the subsequent dynamics of the system. The eigenvalues of this 2T-periodic fixed point are shown in Fig. 4 and it shows that close to the bifurcation point it has two eigenvalues close to 1. One eigenvalue is close to 1 due to the imminent SN bifurcation and the other from the PD bifurcation. As i_{ref1} is increased, these two eigenvalues approach each other, merge and become complex conjugate – within a very small parameter range.

With this change, the fixed point corresponding to the 2T-periodic orbit becomes an unstable focus. Trajectories starting close to this fixed point would spiral out, finally converging on a closed loop – a torus. Since there are two branches of a 2T-periodic orbit, this would create a two-loop torus. The outward motion is arrested since in such a system the state variables cannot assume infinite values. Moreover, the duty ratio saturation also imposes a limit on the state variables.

The aforementioned analysis can further be clarified by creating the loci of the fixed point corresponding to T-periodic and 2T-periodic orbits. Fig. 5a shows the bifurcation diagram when the inductor current i_{L1} is plotted and Fig. 5b shows it when the capacitor voltage of v_{C1} is plotted. This brings forth a peculiarity of this particular system. Both apparently look like PD (in two different directions), which is misleading. These diagrams are in fact projections of a high-dimensional state space, and the situation becomes clear only when 3D perspective view is taken. Fig. 5c shows this view. It shows that two different branches of the T-periodic orbits coexist for $i_{ref1} \in (40, 46.1)$ A. One branch with $D_1 < D_2$ is stable while the other one with $D_1 > D_2$ is a saddle.

At $i_{ref1} \simeq 46.1$, both orbits collide and disappear through an SN bifurcation. At another critical parameter value slightly below the SN bifurcation point, the two branches of the 2T-periodic orbit are born being a foci with unstable complex conjugate eigenvalues. These are responsible for the creation of the two-loop torus shown previously in Fig. 3b.

Keeping in mind that the fixed points correspond the sampled values of the state variables at the end of the switching cycles, it can also be observed that the inductor current waveforms for both
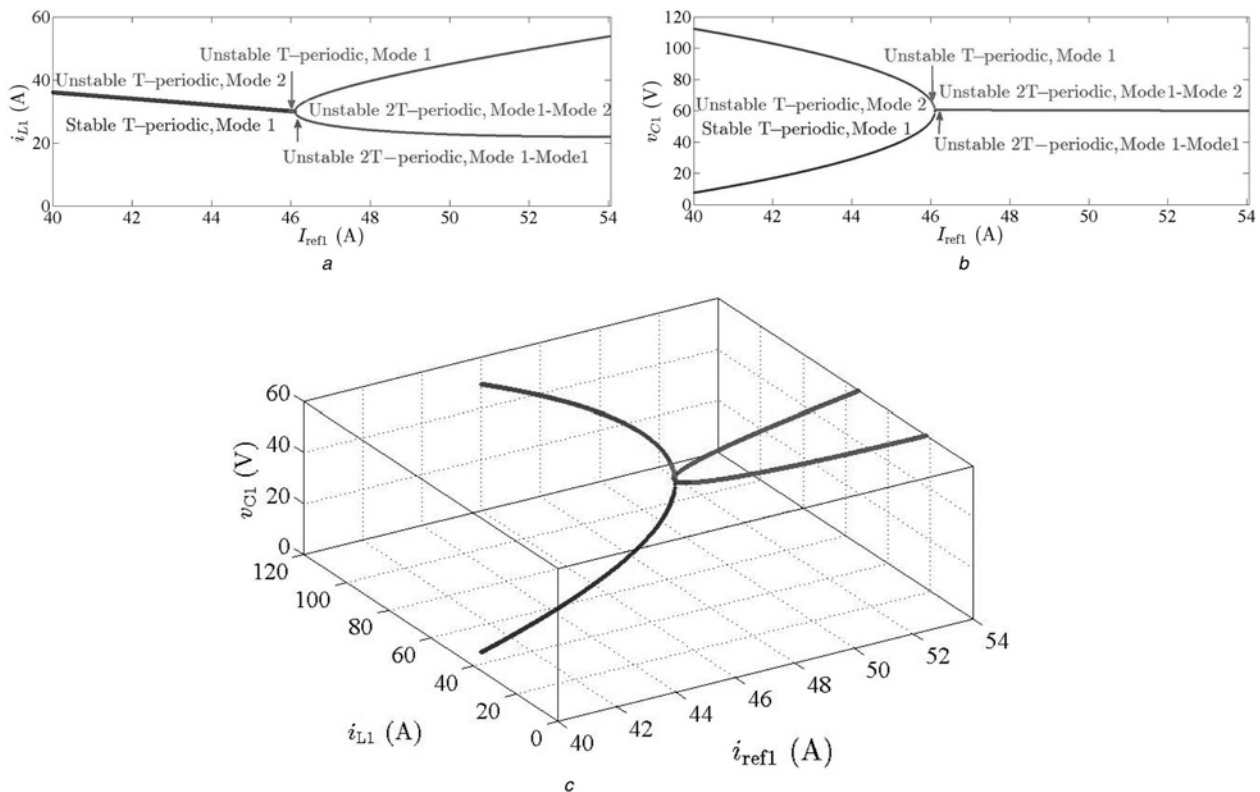

Fig. 5 *Loci of the fixed points corresponding to the T-periodic and 2T-periodic orbits as the parameter i_{ref1} is varied*

a $i_{L1}(T)$ and $i_{L1}(2T)$ against i_{ref1}
b $v_{C1}(T)$ and $v_{C1}(2T)$ against i_{ref1}
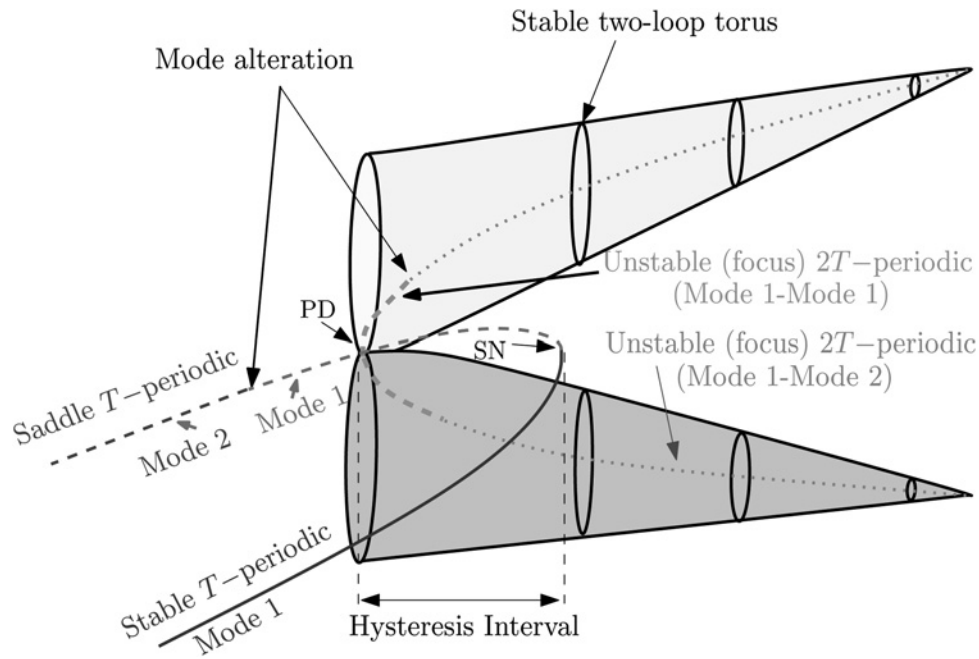*c* Three-dimensional view of the bifurcation diagram

Fig. 6 *Complete scenario of the bifurcation patterns. Within the hysteresis interval two stable attractors coexist: a torus and a T-periodic orbit*

operating modes are characterised by practically the same crest value $i_{L1}(0) = i_{L1}(T)$ and by the same peak value $i_{L1}(D_1T) = i_{ref1} - m_{a1}D_1T$, but with two different values of the duty cycle D_1. Therefore, the SN bifurcation is more visible in the voltage diagram (Fig. 5b) while PD is more visible in the current diagram (Fig. 5a).

Fig. 6 schematically illustrates the complete scenario where the change of operation mode, SN and PD instabilities are shown, along with the torus that is born out of the $2T$-periodic orbit and the hysteresis interval which exists due to to the coexistence of different steady-state solutions for a set of parameter values. The parameter difference between the PD and SN bifurcations has been exaggerated to make the sequence of events clearer.

Fig. 7 shows the two-parameter stability curves in the (v_g, i_{ref1}) and (i_{ref2}, i_{ref1}) parameter planes. In this figure, the desired stable region is explicitly shown after predicting the boundary of the undesired behaviour. On the basis of these kinds of figures, one can appropriately select the parameter values of the system to avoid instabilities.

It can be observed that the boundaries are very close to each other. Even though the stability boundaries are close, they do not coincide. This coincidence is not a numerical artefact. For realistic parameter values the bifurcation curves just happen to be close. Using non-realistic values for the parameters such as larger clock period or larger values of parasitic resistances r_{L1} and r_{C1}, we have checked that the boundaries drift further apart.
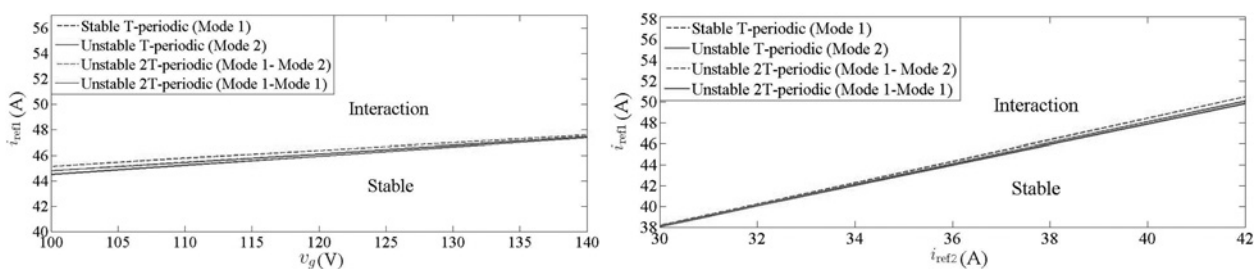
5 Experimental validation

5.1 System description

In this section, we experimentally validate the interaction of the slow-scale and fast-scale bifurcation phenomena reported and analysed in the previous section. For that purpose, an experimental prototype was built. A detailed schematic circuit diagram of the implemented system is shown in Fig. 8. The implemented circuit uses the parameter values shown in Table 3. The switching frequency in both stages was fixed at $f_s = 50$ kHz.

In the first stage, the switch is implemented by the metal–oxide–semiconductor field-effect transistor (MOSFET) IRF840A and the diode MBR40250TG. In the second stage, the devices used are the MOSFET IPB320N20N3 and the diode MBR20200CTG. The control stage includes two different parts, one for each stage. The first part consists of a set-reset (S-R) latch and a comparator LM319 for generating the switching signal u_1. The comparator compares the inductor current i_{L1} with the current reference i_{ref1}. No compensating ramp is used in the first stage. The current controller in the second stage consists of TL082IN device performing the current compensation with appropriate passive components. The zero of the compensator is given by the resistance $R_z = 1$ kΩ and the capacitance $C_z = 100$ nF. The comparator used to decide the switching signal u_2 in the second stage is LM319N.
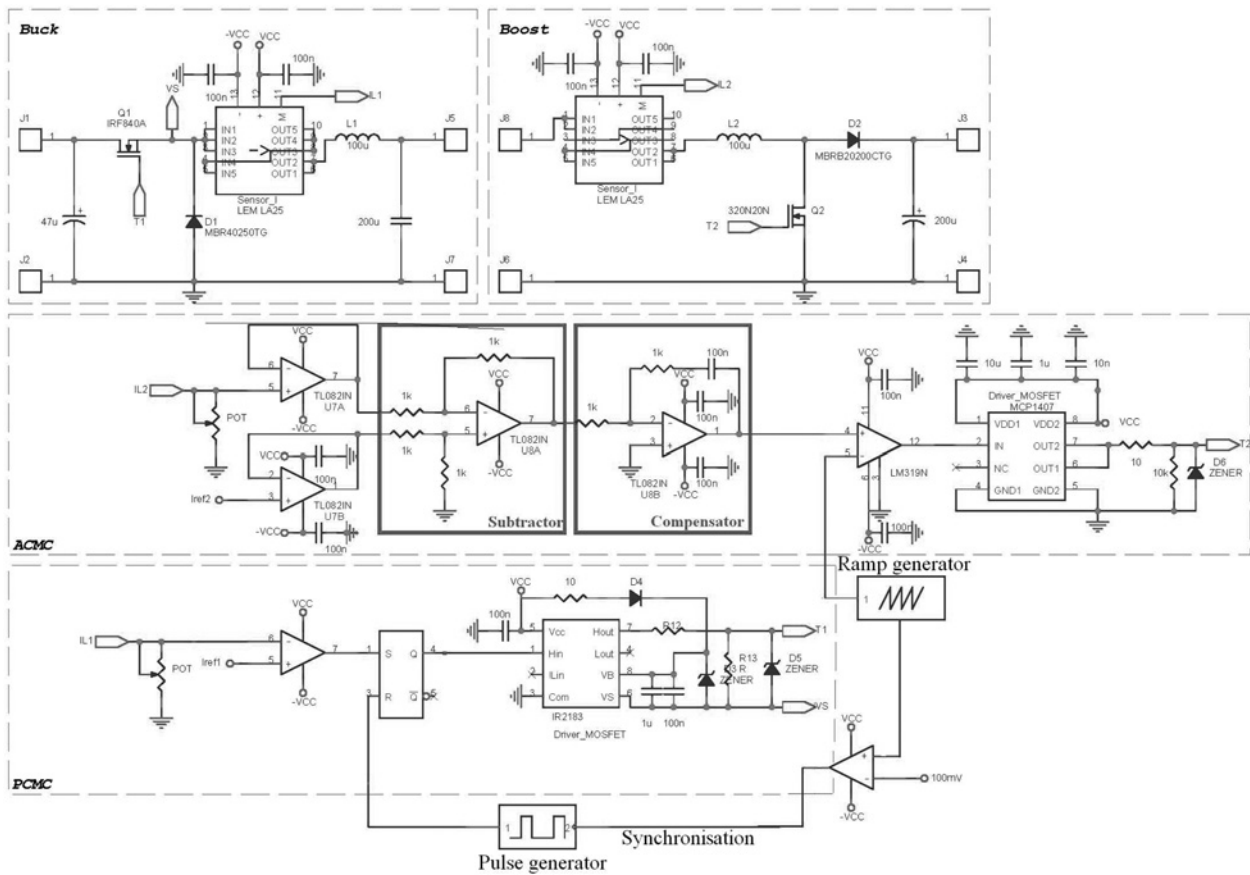

Fig. 7 *Two-parameter stability curves in the parameter spaces (v_g, i_{ref1}) and (i_{ref2}, i_{ref1}) corresponding to different T-periodic orbits*

Fig. 8 *Schematic circuit diagram of the implemented circuit showing the two power stage circuits and their controllers*

Table 3 Used parameter values in the experimental prototype

L_1, r_{L1}	C_1, r_{C1}	L_2, r_{L2}	C_2, r_{C2}	R	W, ω_z, ω_p
100 µH, 20 mΩ	200 µF, r_{C1} = 5 mΩ	30 µH, 10 mΩ	200 µF, 18 mΩ	5 Ω	78.5, 10, 157 krad/s

The synchronisation between the two stages is guaranteed by generating the clock signal in the first stage from the external ramp signal of the second stage. For that purpose, the external ramp signal is compared using an LM319 comparator with a small constant voltage (CONST = 100 mV). The generated pulses are then applied to the set input of the S-R latch in the first stage. The drivers utilised are MCP1407 for the first stage and IR2183 for the second stage. The current sensor in both stages is LA25-NP. The system is fed by a Multimetrix XA3033 power supply. The bandwidth (150 kHz) of the current sensor is used as a second pole of the compensator in the second stage.

5.2 Circuit performance

The circuit parameters are fixed as in Table 3. The current reference in the first and second stages are i_{ref1} = 4.2 A and i_{ref2} = 3.75 A, respectively. To explore the different dynamical behaviours of the system, the input voltage v_g in the first stage is varied. For instance, for v_g = 20 V, the system exhibits a stable T-periodic regime. If v_g is decreased to ~18 V, the system loses its stability. The time-domain waveforms before and after the loss of stability, obtained from numerical simulations and experimental measurements, are shown in Fig. 9. It can be clearly observed that there is an interaction of fast-scale and slow-scale instabilities in Figs. 9c and d similar to the one obtained in Section 3 (Fig. 2) by only numerical simulations using a different set of parameter values.

6 Conclusions

Over the past couple of decades, cascade-interconnected converter systems have become common in DPSs in a broad range of applications, because the desired output voltage/current can be obtained with higher efficiency than in single-stage systems and a specified variation in output voltage can be realised faster and more precisely. However, the added complexity and higher state-space dimension may induce newer types of instabilities, which need to be understood in order to produce proper design guidelines. In this paper, we have investigated the cascade connection of a buck and a boost converter under current mode control, and have identified such instabilities. We show that, as a parameter is varied, such a system may abruptly transit from a stable T-periodic behaviour to a two-loop torus, exhibiting a new type of interaction between fast-scale and slow-scale dynamics. We show that dynamics of this system is governed by a complex interplay between an SN bifurcation and a sub-critical period-doubling bifurcation occurring on an unstable periodic orbit. The torus is created when the unstable $2T$-periodic orbit is born unstable with two complex conjugate eigenvalues. Subsequently, as the bifurcation parameter is varied, the two loops become disconnected forming two separated loops in the state space. The phenomena reported in this paper can take place for all cascade-interconnected converter systems in which the first stage is a buck or an equivalent converter and the second stage is a power conversion system with a tightly regulated input current. Our future work will deal with the non-linear analysis of other
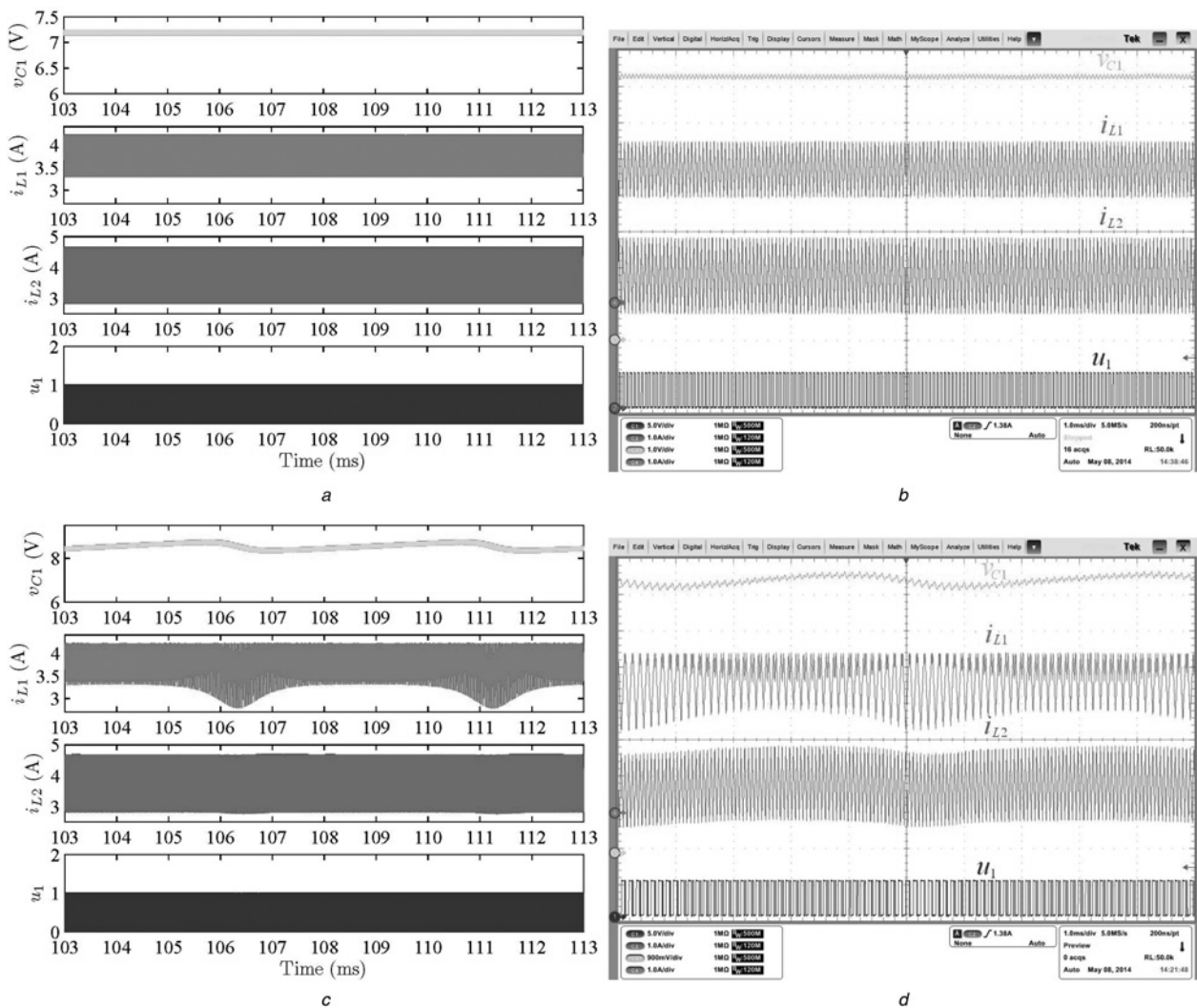
Fig. 9 *Waveforms of the cascaded system showing the interaction between fast- and slow time-scale oscillations before and after losing stability*

a, b Before: ($v_g \simeq 20$ V)
c, d After: ($v_g \simeq 17.2$ V)
Left: numerical simulation; right: experimental validation; and current references: $i_{ref1} = 4.2$ A, $i_{ref2} = 3.75$ A

more complex interconnected converter topologies for DPSs applications.

7 Acknowledgments

8 References

1 Fahimi, B., Kwasinski, A., Davoudi, A., *et al.*: 'Powering a more electrified planet', *IEEE Power Energy Mag.*, 2011, **11**, (2), pp. 54–64
2 Middlebrook, R.D.: 'Input filter consideration in design and application of switching regulators'. Industry Applications Society Annual Meeting, 1976, pp. 366–382
3 Veerachary, M., Sudhakar, S.B.: 'Stability analysis of cascaded DC–DC power electronic system', *IEEJ Trans. Electr. Electron. Eng.*, 2009, **4**, pp. 763–770
4 Kwasinski, A., Onwuchekwa, C.N.: 'Dynamic behavior and stabilization of DC microgrids with instantaneous constant-power loads', *IEEE Trans. Power Electron.*, 2011, **26**, (3), pp. 822–834
5 Zhang, H., Yang, X., Ma, X., *et al.*: 'Theoretical and experimental investigation of bidirectional Hopf bifurcations in cascade DC–DC buck converters', *Math. Comput. Simul.*, 2011, **82**, (4), pp. 540–557
6 Stramosk, V., Benadero, L., Pagano, D.J., *et al.*: 'Sliding mode control of interconnected power electronic converters in DC microgrids'. 39th Annual Conf. of the IEEE Industrial Electronics Society, IECON'2013, Vienna, Austria
7 Banerjee, S., Verghese, G.C. (EDs.), Nonlinear phenomena in power electronics: 'Attractors, bifurcations chaos, and nonlinear control' (IEEE Press, New York, 2001)
8 Tse, C.K.: 'Complex behavior of switching power converters' (CRC Press, Boca Raton, USA, 2003)
9 Lu, W.-G., Zhou, L.-W., Luo, Q.-M., *et al.*: 'Non-invasive chaos control of dc–dc converter and its optimization', *Int. J. Circuit Theory Appl.*, 2011, **39**, (2), pp. 159–174
10 Zhusubaliyev, Z.-T., Mosekilde, E., Yanochkina, O.O.: 'Torus-bifurcation mechanisms in a DC/DC converter with pulsewidth-modulated control', *IEEE Trans. Power Electron.*, 2011, **26**, (4), pp. 1270–1279
11 Fang, C.C.: 'Saddle-node bifurcation in the buck converter with constant current load', *Nonlinear Dyn.*, 2012, **69**, (4), pp. 1739–1750
12 Giaouris, D., Banerjee, S., Zahawi, B., *et al.*: 'Stability analysis of the continuous conduction mode buck converter via Filippov's method', *IEEE Trans. Circuits Syst. I, Fundam. Theory Appl.*, 2008, **55**, (2), pp. 543–550
13 Giaouris, D., Maity, S., Banerjee, S., *et al.*: 'Application of Filippov method for the analysis of subharmonic instability in DC–DC converters', *Int. J. Circuit Theory Appl.*, 2009, **37**, (8), pp. 899–919
14 Deivasundari, P., Uma, G., Poovizhi, R.: 'Analysis and experimental verification of Hopf bifurcation in a solar photovoltaic powered hysteresis current-controlled cascaded-boost converter', *IEE IET Power Electron.*, 2013, **6**, (4), pp. 763–773
15 Deivasundari, P., Uma, G., Santhi, R.: 'Experimental verification of Hopf bifurcation in pulse-width modulated inverter fed cage induction motor drive system', *IEE IET Power Electron.*, 2013, **7**, (2), pp. 340–349
16 Gavagsaz-Ghoachani, R., Martin, J., Pierfederici, S., *et al.*: 'DC power networks with very low capacitances for transportation systems: dynamic behavior analysis', *IEEE Trans. Power Electron.*, 2013, **28**, (12), pp. 5865–5877

17 Chen, Y., Tse, C.K., Qiu, S.S., *et al*.: 'Coexisting fast-scale and slow-scale instability in current-mode controlled DC/DC converters: analysis, simulation and experimental results', *IEEE Trans. Circuits Syst. I, Regul. Pap.*, 2008, **55**, (10), pp. 3335–3348

18 Zhou, G.-H., Xu, J.-P., Bao, B.-C.F., *et al*.: 'Complex dynamics and fast-slow scale instability in current-mode controlled buck converter with constant current load', *Int. J. Bifurcation Chaos*, 2013, **23**, (4), p. 1350062, (15 pages)

19 Giaouris, D., Banerjee, S., Imrayed, O., *et al*.: 'Complex interaction between tori and onset of 3-frequency quasiperiodicity in a current mode controlled boost converter', *IEEE Trans. Circuits Syst. I*, 2012, **59**, (1), pp. 207–214

20 Giaouris, D., Banerjee, S., Stergiopoulos, F., *et al*.: 'Foldings and grazings of tori in current controlled interleaved boost converters', *Int. J. Circuit Theory Appl.*, 2013, **42**, pp. 1080–1091

21 Huang, Y., Iu, H.C., Tse, C.K.: 'Boundaries between fast- and slow-scale bifurcations in parallel-connected buck converters', *Int. J. Circuit Theory Appl.*, 2008, **36**, (5), pp. 681–695

22 Choi, B., Cho, B.H., Hong, S.-S.: 'Dynamics and control of dc-to-dc converters driving other converters downstream', *IEEE Trans. Circuits Syst. I, Fundam. Theory Appl.*, 1999, **46**, (10), pp. 1240–1248

23 Leyva-Ramos, J., Ortiz-Lopez, M.G., Diaz-Saldierna, L.H., *et al*.: 'Average current controlled switching regulators with cascade boost converters', *IEE IET Power Electron.*, 2011, **4**, (1), pp. 1–10

24 Ortiz-Lopez, M.G., Leyva-Ramos, J., Carbajal-Gutierrez, E.E., *et al*.: 'Modelling and analysis of switch-mode cascade converters with a single active switch', *IEE IET Power Electron.*, 2008, **1**, (4), pp. 478–487

25 El-Sayed Ahmed, M., Orabi, M., Abdelrahim, O.M.: 'Two-stage micro-grid inverter with high-voltage gain for photovoltaic applications', *IEE IET Power Electron.*, 2013, **6**, (9), pp. 1812–1821

26 El Aroudi, A., Giaouris, D., Martinez-Salamero, L., *et al*.: 'Bifurcation behavior in switching converters driving other downstream converters in dc distributed power systems applications'. MEDYNA'2013: First Euro-Mediterranean Conf. on Structural Dynamics and Vibroacoustics, Marrakech Morocco, Marrakech Morocco, 2013